Nanoscale

PAPER

View Article Online
View Journal

Cite this: DOI: 10.1039/d5nr05277g

Precursor effects and formation mechanism of polyol-synthesized thermoelectric Bi_2Te_3†

Madison Donohoe, ‡[a] Tristan Licskai, ‡[a] Ehsan Niknam, [a] Abdeljalil Assoud, [a] Tianze Zou, [b] Jan Kycia [b] and Holger Kleinke *[a]

Received 16th December 2025,
Accepted 26th March 2026

DOI: 10.1039/d5nr05277g

rsc.li/nanoscale

Polyol synthesis offers a controllable and scalable approach for producing high-performance thermoelectric materials such as bismuth telluride (Bi_2Te_3), providing more control over crystal growth and microstructure compared to conventional solid-state methods. The chemical nature of the selected precursors can strongly influence the reaction pathways, phase evolution, and resulting material properties. In this work, two polyol synthesis routes using Bi_2O_3 and $Bi(NO_3)_3{\cdot}5H_2O$ as bismuth precursors were systematically investigated to evaluate their influence on the structural evolution and thermoelectric performance of Bi_2Te_3. Comparative characterization and transport measurements reveal clear precursor-dependent variations in microstructure and anisotropic charge transport. Despite being undoped, both materials exhibit strong thermoelectric performance with the nitrate-derived sample achieving a peak figure of merit of zT = 1.27 at 432 K, and the oxide-derived material reaching zT = 1.10 at 333 K. Moreover, analysis of the nitrate route revealed the formation of a previously unreported bismuth complex, $Bi_3(C_2H_4O_2)_4NO_3$. Overall, these findings advance the mechanistic understanding of Bi_2Te_3 formation in polyol synthesis and highlight the importance of precursor selection as a key parameter for tailoring microstructure and optimizing thermoelectric performance.

Introduction

Global warming and the growing global demand for energy have intensified the pursuit of sustainable energy technologies and efficient waste heat recovery strategies. One promising approach involves the use of thermoelectric generators (TEGs), which are solid-state devices capable of directly converting temperature gradients into electrical energy through the Seebeck effect. Due to their reliability, scalability, and environmental advantages, TEGs are increasingly being explored for a wide range of applications in both industrial and consumer sectors.[1–7]

The performance of a thermoelectric (TE) material is quantified by the dimensionless figure of merit, zT, defined in eqn (1):

$$zT = \frac{\sigma \cdot S^2}{\kappa} T \quad (1)$$

where σ is the electrical conductivity, S is the Seebeck coefficient, κ is the total thermal conductivity (comprising of both electronic, κ_e, and lattice, κ_l, components), and T is the temperature. Maximizing zT requires careful optimization of these interdependent parameters, so that thermal conductivity is minimized to maintain a temperature gradient, electrical conductivity is increased to enhance charge transport, and the Seebeck coefficient is maximized to generate a larger thermoelectric voltage.

Bismuth telluride (Bi_2Te_3) remains the most extensively utilized TE material for waste heat recovery in the low- to room-temperature range due to its superior performance near ambient conditions.[8,9] It crystallizes in a rhombohedral structure with the $R\bar{3}m$ space group and consists of quintuple layers stacked along the c axis in the sequence Te(1)–Bi–Te(2)–Bi–Te(1).[10] Due to its layered structure, charge carrier transport properties can differ significantly when measured parallel (∥) or perpendicular (⊥) to the a,b crystal plane, necessitating careful consideration of anisotropic effects.[11]

Conventionally, Bi_2Te_3 is synthesized by melting stoichiometric amounts of the elemental constituents in sealed silica ampoules, often followed by mechanical pulverization (*e.g.*, ball milling) and pelletization through techniques such as hot pressing or spark plasma sintering.[12] While this approach yields high-density bulk materials, it offers limited control over crystal growth, morphology, and microstructure, which

[a]Department of Chemistry and Waterloo Institute for Nanotechnology, University of Waterloo, 200 University Ave W., Waterloo, Ontario N2L 3G1, Canada. E-mail: kleinke@uwaterloo.ca
[b]Department of Physics and Astronomy and Institute for Quantum Computing, University of Waterloo, Waterloo, Ontario, N2L 3G1, Canada
†Themed Collection: Thermoelectric Energy Conversion
‡These authors contributed equally.

strongly influence carrier mobility, defect concentration, and ultimately thermoelectric performance.[13] In contrast, solution-based synthesis routes, such as the polyol process, have recently gained attention as scalable and tunable alternatives.[14,15] These methods enable improved control over particle size, shape, and crystallographic orientation under milder conditions, thereby offering more opportunities for optimizing the microstructure and enhancing charge transport in Bi_2Te_3-based materials.[16]

In the polyol synthesis route, soluble precursors are typically refluxed in ethylene glycol (EG), which acts as both the solvent and reducing agent. The choice of bismuth and tellurium precursors can vary depending on solubility, cost, and redox behavior. Sodium tellurite(IV) (Na_2TeO_3) is a commonly used tellurium source, where tellurium exists in the +4 oxidation state and must be reduced by EG to Te^{2-} to form Bi_2Te_3. Bismuth(III) oxide (Bi_2O_3) is frequently selected as the bismuth source, as it readily dissolves in EG at room temperature and already possesses the required +3 oxidation state. For instance, Gayner *et al.* used these starting materials to synthesize Bi_2Te_3 *via* polyol and achieved a peak "*zT*" of 1.30 at 450 K and an average "*zT*" of 1.14 between 300 K and 500 K;[17] quotation marks are used here to indicate that anisotropy effects were not explicitly accounted for in those measurements, leading to not quite accurate "*zT*" values. The overall reaction using these precursors can be represented as follows:

$$Bi_2O_3 + 3Na_2TeO_3 + 9HO - H_2C - CH_2 - OH \rightarrow Bi_2Te_3 + 9HO - H_2C - CHO + 6NaOH + 6H_2O.$$

Bismuth(III) nitrate pentahydrate ($Bi(NO_3)_3{\cdot}5H_2O$) is an alternative Bi^{3+} precursor that also dissolves readily in EG. For instance, Kimberly *et al.* achieved a peak *zT* of 0.75 at 425 K and an average *zT* of 0.65 between 300 K and 500 K using it as a bismuth source in polyol Bi_2Te_3 synthesis.[18] The corresponding overall reaction using $Bi(NO_3)_3{\cdot}5H_2O$ is shown below:

$$2Bi(NO_3)_3 \cdot 5H_2O + 3Na_2TeO_3 + 9HO - H_2C - CH_2 - OH \rightarrow Bi_2Te_3 + 9HO - H_2C - CHO + 6NaNO_3 + 19H_2O.$$

Although both precursor systems have been used in previous studies, there was little exploration of the mechanistic pathways leading from precursor reduction and nucleation to the formation of crystalline Bi_2Te_3. A deeper understanding of these reaction mechanisms is critical for optimizing stoichiometry control, dopant incorporation, and microstructural evolution in solution-based Bi_2Te_3 synthesis.

In this study, two polyol-based synthesis routes for Bi_2Te_3 were systematically investigated, employing Bi_2O_3 and Bi $(NO_3)_3{\cdot}5H_2O$ as bismuth precursors. These samples are hereafter referred to as BO and BN, respectively. Particular attention was given to elucidating the reaction mechanism of the BN pathway, which involves the formation of a previously unreported bismuth complex, namely $Bi_3(C_2H_4O_2)_4NO_3$. The identification of this complex provides new insight into the coordination chemistry of bismuth species in ethylene glycol and its role in controlling nucleation and growth of Bi_2Te_3 nano/microcrystals. In addition to mechanistic characterization, the structural and thermoelectric properties of the BO and BN Bi_2Te_3 samples were examined and compared. The analysis includes consideration of anisotropic transport behavior, arising from the inherently layered rhombohedral structure of Bi_2Te_3, to better understand how Bi precursor selection influences microstructural orientation and resulting thermoelectric performance.

Experimental

Material synthesis and preparation

To prepare 8 g of the BO sample, stoichiometric quantities of bismuth(III) oxide (4.656 g Bi_2O_3, 99.99%, Sigma-Aldrich) and sodium tellurite(IV) (6.642 g Na_2TeO_3, 97%, Thermo Scientific) were added to a two-necked round-bottom flask containing 100 mL of ethylene glycol ($(CH_2OH)_2$, 99%, Oakwood Chemical). The mixture was magnetically stirred and refluxed at 463 K under a nitrogen atmosphere for a total of 10 hours, divided into two consecutive 5-hour heating periods. Aliquots were collected at 1-hour intervals during each heating stage to monitor reaction progress, and an additional aliquot was taken prior to the second reflux cycle to confirm the stability of the reaction mixture during the interim period. An analogous procedure was used for the BN sample, substituting Bi_2O_3 with bismuth(III) nitrate pentahydrate (9.692 g Bi $(NO_3)_3{\cdot}5H_2O$, 98%, Alfa Aesar). The reaction was refluxed for a total of 20 hours, divided into two consecutive 10-hour heating periods, with aliquots collected at identical intervals to enable direct comparison of the two synthesis pathways.

After cooling to room temperature, the 1-hour aliquots and bulk samples were transferred into 15 mL and 50 mL centrifuge tubes, respectively, using deionized (DI) water. The suspensions were centrifuged at 6000 rpm for 1 min using an Eppendorf Centrifuge 5804 to separate the precipitated solids. The supernatant was decanted, and the recovered solids were sequentially washed with DI water (9000 rpm, 5 min) and ethanol (8000 rpm, 5 min). The alternating DI water/ethanol washing procedure was repeated two additional times to ensure the complete removal of solvent and by-products.

After drying, each bulk powder was loaded into a 12.7 mm graphite die and hot-pressed using an OXY-GON Hot Press at 673 K under an applied pressure of 46 MPa for 2 h in an ultra-high-purity (99.999%) argon atmosphere. Thin graphite foils were placed between the sample and graphite plungers to prevent adhesion, and the residual graphite was subsequently removed by gentle sanding. To enhance pellet densification, the hot-pressed pellets were then cold-pressed in a stainless-steel die using a two-column Weber-Pressen press at 474 MPa for 5 min, followed by a second hot-pressing step under identical temperature and pressure conditions.

Characterization and property measurements

Powder X-ray diffraction (PXRD) was employed to identify crystalline phases, assess phase purity, and monitor structural

evolution in the 1-hour aliquots, final powders, and hot-pressed pellets. Diffraction patterns were collected using a Malvern PANalytical Aeris instrument equipped with a Cu-Kα radiation (λ = 1.5406 Å) source operating at 40 kV and 15 mA. PXRD patterns were acquired over a 2θ range of 10°–70° with a step size of 0.022° and an exposure time of 2 s per step, for a total scan time of approximately 1.5 h per sample. Instrumental alignment was verified using a silicon standard prior to data collection. The obtained diffraction data were analyzed and refined using GSAS-II for phase identification and lattice parameter determination.[19]

Surface morphology and elemental analysis of the samples were obtained using transmission electron microscopy (TEM) and scanning electron microscopy (SEM) coupled with energy-dispersive X-ray spectroscopy (EDS). TEM was done using a JEOL F200 Analytical instrument with a SpecPorter auto sample loader and a Gatan OneView camera. The samples were sonicated in isopropyl alcohol, transferred to Au TEM grids, and cleaned using a PIE Scientific Tergeo EM Plasma cleaner. Data analysis was completed with the Gatan Digital Micrograph software. The SEM imaging was performed on a Zeiss LEO 1530 instrument equipped with a Schottky-type field-emission electron gun. Images were captured using back-scattered electron (BSE) and secondary electron (SE) detectors at a voltage of 20 kV. Additionally, EDS mapping and line analyses were employed to confirm elemental distribution and stoichiometry across the sample surfaces with an instrumental uncertainty of approximately ±5%.

The Archimedes method was used to determine the densities (ρ) of the pellets with a Sartorius TDK01 density determination kit. Furthermore, the specific heat capacity (C_p) was estimated using the Dulong–Petit law, which has been demonstrated to provide a reliable approximation for Bi_2Te_3-based materials in the low-temperature range.[20,21] Thermal diffusivity (D) measurements were performed under an ultra-high purity (99.999%) argon environment using a Discovery Laser Flash 1200 instrument (TA Instruments) over the temperature range of 298 K to 523 K. Thermal conductivity (κ) was subsequently calculated according to eqn (2):

$$\kappa = D \cdot C_P \cdot \rho. \quad (2)$$

The overall measurement uncertainty of κ was approximately ±5%.[22]

The pellets were then cut into bars with approximate dimensions of 7 mm × 2 mm × 2 mm using a diamond-coated copper cutting wheel. These bars were used to measure the Seebeck coefficient and electrical conductivity in an ultra-high purity (99.999%) helium atmosphere using a Ulvac-Riko ZEM-3 instrument over the temperature range of 298 K to 523 K. The estimated experimental uncertainties for the Seebeck coefficient and electrical conductivity were approximately ±3% and ±5%, respectively.[23] Finally, zT was calculated according to eqn (1) with a total experimental error of approximately ±10%.

Lastly, Hall effect measurements were performed to determine the Hall charge carrier concentration and mobility. Rectangular bars (~7 mm × 2 mm × 1 mm) were cut from the same pellets used for Seebeck coefficient and electrical conductivity measurements to ensure consistency. Each bar was mounted on a sample holder equipped with pogo-pin contacts. Electrical conductivity was measured using a four-probe AC technique. An SR830 lock-in amplifier supplied the current and measured the voltage, while a second lock-in amplifier monitored the current through a 10 Ω series resistor. Hall resistance was determined by measuring the Hall voltage under an applied 5 mA AC current and an alternating magnetic field of ±0.5 T. The Hall signal was amplified using a PAR 190 transformer and detected by the lock-in amplifier that provides the current. Sample temperature was maintained near room temperature using a PID-controlled Peltier stage. Voltage measurement noise was below ±1%, and the overall uncertainties in calculated mobility and carrier concentration were estimated to be approximately ±3%.

Characterization of the $Bi_3(C_2H_4O_2)_4NO_3$ complex

The $Bi_3(C_2H_4O_2)_4NO_3$ complex was characterized by single-crystal X-ray diffraction (SCXRD) at room temperature using a Bruker Kappa APEX II CCD instrument with Mo-Kα radiation (λ = 0.71073 Å). A colorless, rectangular crystal was mounted on a thin glass fiber, and full data coverage was achieved by scanning ω and ϕ in 0.36° increments with 40 s exposure per frame, following an APEX II–generated data strategy. Collected data were corrected for Lorentz and polarization effects, and absorption corrections were applied using SADABS (multi-scan method). The crystal structure was solved using direct methods and refined by full-matrix least-squares on F^2 with SHELXTL. Non-hydrogen atoms were refined anisotropically, while hydrogen atoms were placed in idealized geometrical positions using a rigid model (C–H = 0.97 Å, $U_{iso}(H) = 1.2U_{eq}(C)$).

Moreover, using Density Functional Theory (DFT) within the Quantum Espresso software,[24–26] the electronic structure of $Bi_3(C_2H_4O_2)_4NO_3$ was computed. The exchange–correlation effects were treated using the Generalized Gradient Approximation (GGA), specifically the Perdew–Burke–Ernzerhof (PBE) functional.[27] A Self-Consistent Field (SCF) calculation with a k-point grid of 2 × 2 × 2 was used to iteratively adjust the electron density until convergence was achieved, determining the ground state electronic structure to an SCF accuracy of 1×10^{-8} Ry. Afterward, the electron density from the SCF calculation was used to perform a Non-Self-Consistent Field (NSCF) calculation using a denser k-point grid of 4 × 4 × 4 to determine the Density Of States (DOS).

Results and discussion

Reaction pathways

To elucidate the precursor-dependent reaction pathways leading to Bi_2Te_3 formation, aliquots were collected hourly over the 10- and 20-hour syntheses for the BO and BN routes, respectively. The corresponding PXRD patterns are shown in

Fig. 1. For the BO synthesis (Fig. 1a), which employs Bi_2O_3 as the bismuth source, the aliquot pattern obtained after just 1 hour already exhibits reflections consistent with the Bi_2Te_3 reference pattern (184631, shown in green) from the Inorganic Crystal Structure Database (ICSD), albeit with low intensity compared to the background due to limited crystallinity and incomplete reaction. Continued reflux leads to progressively better-defined Bi_2Te_3 reflections without the appearance of additional phases, consistent with increasing crystallinity and a direct transformation to phase-pure Bi_2Te_3 under the chosen conditions.

In contrast, the BN synthesis, which employs $Bi(NO_3)_3{\cdot}5H_2O$ as the bismuth precursor, proceeds through a more complex reaction pathway. During the initial 1–3 hours, the PXRD patterns primarily correspond to Bi_2TeO_5 (ICSD: 36446, shown in orange), a well-known intermediate in polyol-based Bi_2Te_3 synthesis.[28–30] This intermediate forms because the ionic bismuth precursor is hydrolyzed more rapidly than the Te^{4+} in Na_2TeO_3 is reduced to Te^{2-}. However, Bi_2TeO_5 does not directly convert to Bi_2Te_3 in this system. Between hours 4–6, prior to the formation of Bi_2Te_3, a previously unreported bismuth-ethylene glycolate-nitrate complex, $Bi_3(C_2H_4O_2)_4NO_3$, emerges (shown in red in Fig. 1). The PXRD reference pattern of this complex was generated in VESTA using the crystal structure obtained from SCXRD in form of its .cif file.[31] This complex exhibits a pronounced characteristic peak at 2θ = 11.64°, which dominates the diffraction pattern and obscures weaker peaks; a magnified view for the 6-hour pattern is provided in SI Fig. S1 to clearly show these additional reflections.

Between hours 7–10 of the BN reaction (shown in purple), the PXRD patterns exhibit reflections corresponding to both $Bi_3(C_2H_4O_2)_4NO_3$ and Bi_2Te_3, indicating the coexistence of these two compounds during this stage of the synthesis. Beyond hour 10, the patterns exclusively match the Bi_2Te_3 reference (ICSD: 184631), with no remaining reflections attributable to $Bi_3(C_2H_4O_2)_4NO_3$, indicating complete conver-

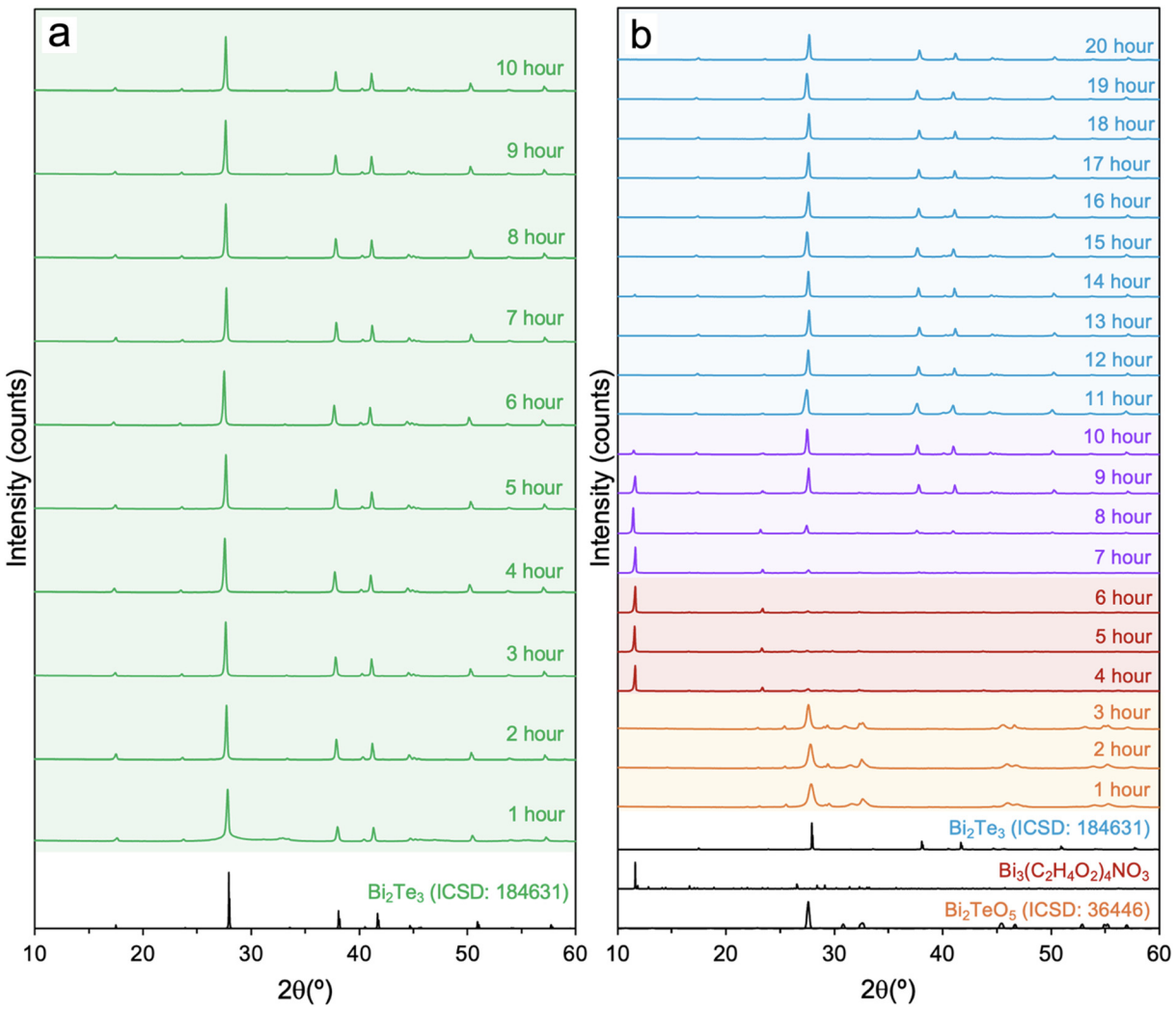

Fig. 1 PXRD of 1-hour aliquots for (a) BO compared to Bi_2Te_3 (ICSD: 184631) and (b) BN compared to Bi_2TeO_5 (ICSD: 36446), $Bi_3(C_2H_4O_2)_4NO_3$, and Bi_2Te_3 (ICSD: 184631).

sion to phase-pure Bi_2Te_3 under extended reflux. The evident differences between the BO and BN reaction pathways highlight the significant influence of bismuth precursor chemistry on the mechanistic progression and phase evolution of polyol-synthesized Bi_2Te_3.

Characterization of $Bi_3(C_2H_4O_2)_4NO_3$

The crystal structure of the previously unreported, neutral bismuth complex, $[Bi_3(C_2H_4O_2)_4][NO_3]$, was determined by SCXRD, and the refined structure is shown in Fig. 2. The compound crystallizes in the monoclinic space group $P2_1/c$ (no. 14) with four formula units per unit cell and refined lattice parameters of a = 7.4599(4) Å, b = 15.1984(9) Å, c = 13.7746(8) Å, and β = 92.892(2)°. Some related complexes with different ligands exist in literature including $[Bi_6(H_2O)(NO_3)O_4(OH)_4](NO_3)_5$ by Lazarini *et al.*[32] and the catalyst $Sb_2(OCH_2CH_2O)_3$ by Biros *et al.*,[33] which both have the same space group and similar layered structures. A full summary of data collection and refinement statistics for $Bi_3(C_2H_4O_2)_4NO_3$ is provided in Table 1. Furthermore, atomic coordinates and anisotropic displacement parameters for all symmetry-independent atoms, along with interatomic bond distances, are listed in SI Tables S1 and S2, respectively.

Each formula unit contains three distinct Bi^{3+} cations, which all adopt distorted octahedral coordination environments with six O atoms (not counting the contacts to NO_3^-), as illustrated in Fig. 3. Charge balance is maintained by a single nitrate anion per formula unit, which are coordinated to the Bi^{3+} centers *via* one or two O atoms at Bi···O distances of approximately 3.0 Å–3.5 Å, as indicated by dashed lines. The dianionic EG ligands coordinate in both chelating and bridging modes to link the Bi^{3+} cations into extended motifs. Bi(1) and Bi(3) each exhibit coordination spheres composed of four bridging ligands and one chelating EG ligand, whereas Bi(2) is coordinated by two bridging and two chelating ligands. The Bi(1)O_6 octahedron displays Bi–O bond lengths ranging from 2.164(4) Å to 2.737(4) Å, corresponding to a maximum bond length difference of 0.57 Å. Bi(2)O_6 shows similar Bi–O distances of 2.139(4) Å to 2.725(4) Å, yielding a bond length difference of 0.59 Å. In contrast, the Bi(3)O_6 unit exhibits a narrower bond-length distribution of 2.184(4) Å to 2.626(4) Å, with the smallest difference being 0.44 Å. These variations reflect differences in the chelating/bridging ligand connectivity and local steric environments around each Bi centre. Lastly, the nitrate anion exists as an almost perfect trigonal planar NO_3^- unit

Table 1 Crystal data and structure refinement of $Bi_3(C_2H_4O_2)_4NO_3$

	$Bi_3(C_2H_4O_2)_4NO_3$
Molecular weight (g mol^{-1})	929.16
Crystal system	Monoclinic
Space group	$P2_1/c$ (no. 14)
a (Å)	7.4599(4)
b (Å)	15.1984(9)
c (Å)	13.7746(8)
β (°)	92.892(2)
Unit cell volume (Å^3)	1559.8(2)
Formula units, Z	4
Temperature (K)	296(2)
Density (g cm^{-3})	3.957
F(000)	1632
Absorption coefficient, μ (mm^{-1})	33.82
Radiation wavelength (Å)	0.71073 (Mo-Kα)
Goodness-of-fit on F^2	1.008
Final R_1 [$I > 2\sigma(I)$][a]	0.027
Final wR_2 [$I > 2\sigma(I)$][a]	0.047
Largest diff. peak and hole (e Å^{-3})	1.96, −1.42

[a] σ = standard deviation.

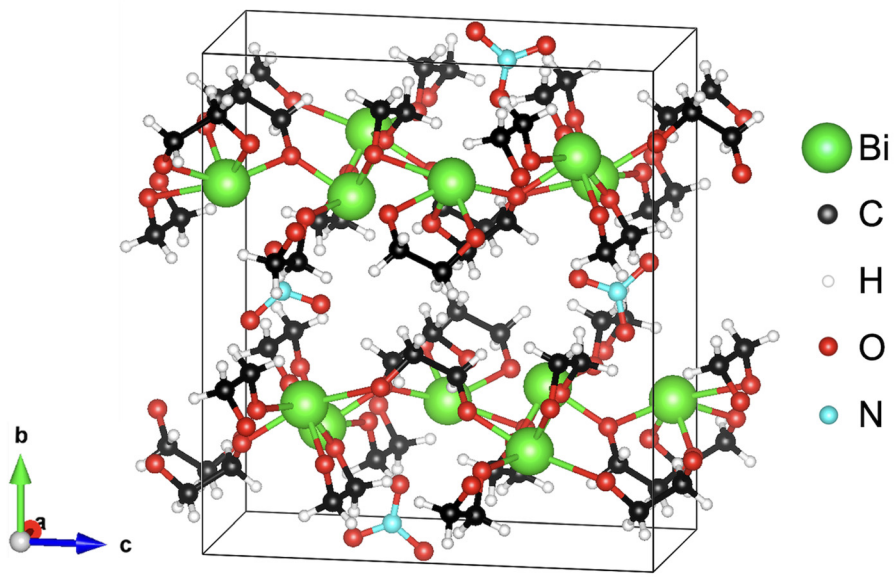

Fig. 2 Crystal structure of $Bi_3(C_2H_4O_2)_4NO_3$.

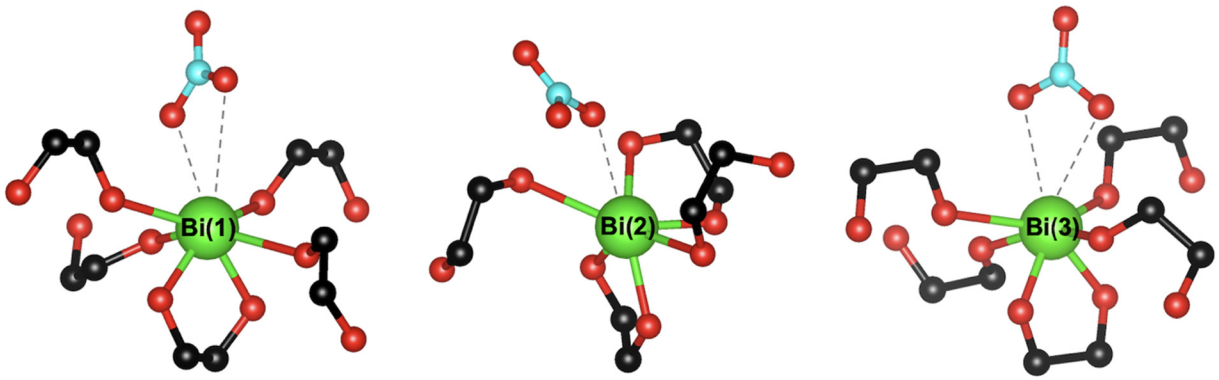

Fig. 3 Bi atom motifs in $Bi_3(C_2H_4O_2)_4NO_3$ (H atoms not shown for clarity).

with N–O bond distances of 1.242(7) Å–1.250(7) Å, consistent with typical nitrate geometries.

The arrangement of the three distinct BiO_6 coordination units give rise to a highly anisotropic, layered framework, as illustrated in Fig. 4. The $Bi(1)O_6$, $Bi(2)O_6$, and $Bi(3)O_6$ distorted octahedra—shown in red, green, and blue, respectively—exhibit different connectivity patterns that define the overall extended structure. Within the *a*,*c* plane, $Bi(3)O_6$ units share edges with both $Bi(1)O_6$ and $Bi(2)O_6$ units, forming extended chains of edge-sharing octahedra. In contrast, $Bi(1)O_6$ and $Bi(2)O_6$ are linked by corner sharing along the *c* axis, producing a stacked, layered arrangement with alternating edge- and corner-sharing connectivity. The nitrate anions, shown in cyan, reside between these Bi–O layers and act as charge-balancing units and hold the layers together. However, they do not fully occupy the interlayer space, resulting in a two-dimensional framework. This layered topology is consistent with the observed distortions in the BiO_6 octahedra and the mixed chelating/bridging coordination modes of the EG-derived ligands.

The electronic DOS was calculated using DFT and is shown in SI Fig. S2. The compound is predicted to be an insulator with a calculated band gap of 3.32 eV, in agreement with its colourless appearance. The valence band is dominated by the 2p orbitals of the O atoms, whereas the conduction band has more contribution from the Bi 6p orbitals. A relatively small O 2p contribution is also observed around 3.5 eV in the conduction region, indicating some degree of Bi–O hybridization. Contributions from C 2p, H 1s, and N 2p atoms are comparatively minor, reflecting their limited involvement in the principal electronic structure.

Precursor-dependent lattice and anisotropy effects

After polyol syntheses, the final BO and BN nano/microcrystalline powders were consolidated into dense pellets under identical hot-pressing conditions to enable subsequent thermoelectric property measurements and to evaluate precursor-dependent effects on the preferred crystallographic orientation. The diameter and thickness of the resulting pellets are reported in SI Table S3. Due to the layered structure of Bi_2Te_3, preferred orientation during sintering is a well-recognized concern as transport properties can differ substantially when measured parallel (∥) *versus* perpendicular (⊥) to the pressing direction.

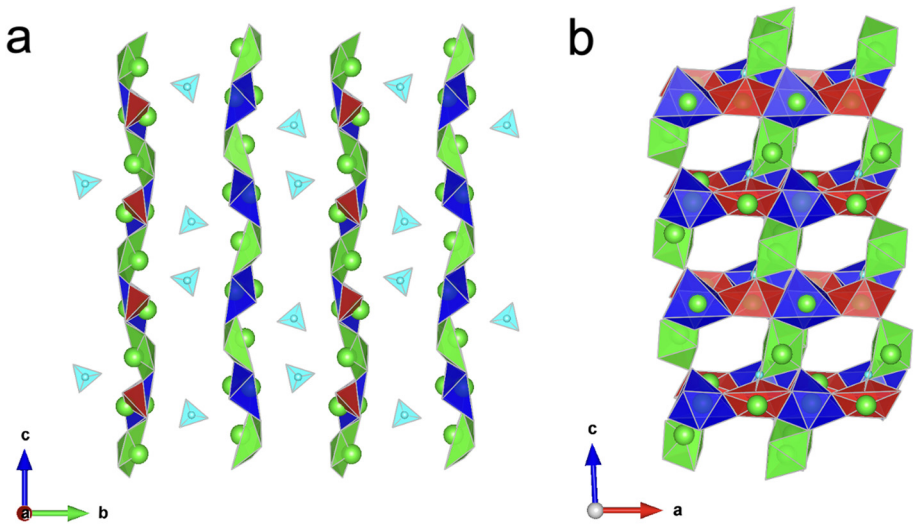

Fig. 4 Layers of $Bi_3(C_2H_4O_2)_4NO_3$ along the (a) *a* axis and (b) *b* axis.

This anisotropy is often amplified in polyol-derived Bi_2Te_3, where the synthesis can yield highly uniform, plate-like crystallites that align readily under pressure.[18,34–36] Given that crystal size and morphology are highly sensitive to synthesis conditions—including the choice of bismuth precursor—the degree of texture induced during hot pressing is expected to differ between the BO and BN samples. Fig. 5 compares the PXRD patterns of each material in its nano/microcrystalline form and after pelletization in both parallel and perpendicular orientations.

In their nano/microcrystalline powder forms in Fig. 5a and after pelletization in Fig. 5b, both BO and BN display diffraction patterns that align closely with the Bi_2Te_3 reference pattern (ICSD: 184631), confirming phase and sample purity. Rietveld refinements using GSAS-II, performed on the materials after hot-press sintering, yield unit cell volumes of 506.19(4) Å^3 and 505.43(4) Å^3 for BN and BO, respectively. This small but measurable difference arises predominantly from a slight elongation of the c axis in BN (30.4697(6) Å) relative to BO (30.4174(1) Å), with the a parameters in much closer agreement. Given the stated uncertainties, this difference is minor, but statistically significant and indicates that precursor chemistry may subtly influence the average crystal lattice (or final composition). Possible contributing factors include slight differences in defect concentration (*e.g.*, Bi_{Te} antisite defects or Te vacancies), microstrain effects associated with crystallization dynamics, or precursor-dependent minor stoichiometry deviations, which could be further evaluated through SEM/EDS and TEM analyses presented later. Overall, both refined volumes remain close to the reported literature value of 508.99 (5) Å^3 for Bi_2Te_3 (ICSD: 184631), supporting that precursor selection does not fundamentally alter the crystal structure. The complete refined lattice parameters, including estimated standard deviations, are summarized in SI Table S4.

While the samples after pelletization in Fig. 5b are pure according to their PXRD diagrams, pronounced changes in relative peak intensities are observed, which indicate a pelletization-induced preferred orientation. In the perpendicular geometry, both BO and BN exhibit notably higher intensities of the (0 0 6), (1 0 10), and (0 0 15) reflections at $2\theta \approx 18°$, 38°, and 45°, respectively, consistent with preferred alignment of the Bi_2Te_3 layers under uniaxial pressing.[11,18] In the parallel geometry, the BO sample has peak intensities much more comparable to those observed for the randomly oriented powder. In contrast, the parallel BN pattern more closely resembles its perpendicular pattern, with only a small decrease in the (0 0 6) and (0 0 15) peak intensities.

To semi-quantitatively evaluate sintering-induced crystallographic texture in the pelletized samples, the Lotgering factor (LF) associated with the (00l) reflections was calculated for both BO and BN pellets measured perpendicular to the pressing axis.[37] The LF was determined according to eqn (3)–(5):

$$LF = \frac{p - p_0}{1 - p_0} \tag{3}$$

$$p = \frac{\sum I(hkl)_{\text{preferred}}}{\sum I(hkl)_{\text{total}}} \tag{4}$$

$$p_0 = \frac{\sum I_0(hkl)_{\text{preferred}}}{\sum I_0(hkl)_{\text{total}}}. \tag{5}$$

In these expressions, $I(hkl)_{\text{preferred}}$ and $I_0(hkl)_{\text{preferred}}$ represent the integrated intensities of reflections belonging to the preferred orientation (here, (00l)) for the textured pellet and randomly oriented reference powder, respectively. Likewise, $I(hkl)_{\text{total}}$ and $I_0(hkl)_{\text{total}}$ denote the summed intensities of all reflections in the corresponding diffraction patterns. The Lotgering factor ranges from 0 to 1, where LF = 0 indicates

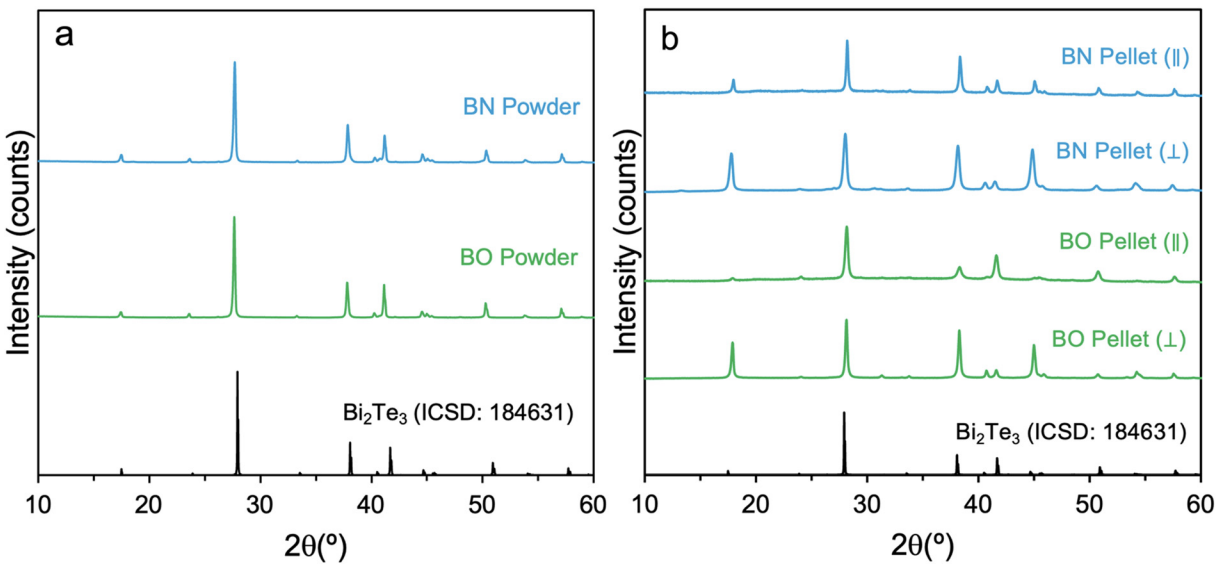

Fig. 5 PXRD comparison of BO and BN to Bi_2Te_3 (ICSD: 184631) for (a) nano/microcrystalline samples and (b) pellets in perpendicular and parallel orientations.

random crystallographic orientation and *LF* = 1 represents perfect alignment along the selected axis. Intermediate values reflect partial texture development, with *LF* values of 0.2–-0.4 generally indicative of moderate preferred orientation. Both BO and BN pellets exhibit moderate (00*l*) preferred orientation in the direction perpendicular to the pressing axis, with BO displaying a slightly higher *LF* = 0.33 compared to 0.30 for BN, indicative of stronger albeit still moderate texture development.

Differences in peak widths in Fig. 5 further distinguish the two samples. In the perpendicular orientation, BO exhibits notably sharper reflections than BN, which may reflect larger coherent domain sizes and/or reduced microstrain. For example, the full width at half maximum (FWHM) of the most intense peak at $2\theta \approx 28°$ is 0.21° for BO compared to 0.35° for BN. Together, these observations demonstrate that the choice of the bismuth precursor influences the microstructural evolution and preferred orientation of polyol-synthesized Bi_2Te_3.

SEM and TEM analyses

To further investigate the structural differences suggested by the PXRD results and to directly examine the morphology of the BO and BN crystallites, both SEM-EDS and TEM analyses were conducted. Quantitative EDS results are summarized in Table 2, with corresponding elemental maps shown in SI Fig. S3. For both precursor routes, the measured atomic percentages (at%) of Bi (BO: 40.4%; BN: 40.8%) and Te (BO: 59.6%; BN: 59.2%) closely match the theoretical stoichiometry expected for Bi_2Te_3 (40% Bi; 60% Te) within estimated error, indicating that precursor chemistry does not introduce detectable deviations in bulk composition. The elemental maps further reveal homogeneous spatial distributions of Bi and Te, with no evidence of precursor-dependent clustering or segregation.

TEM images in Fig. 6 provide higher-resolution insight into the particle morphology of the BO and BN samples, complementing the structural differences inferred from PXRD. The BO crystallites (Fig. 6a) appear as relatively uniform, thin hexagonal platelets with well-defined facets and occasional nanopores. This morphology is characteristic of layered Bi_2Te_3 grown under homogeneous nucleation conditions and is consistent with the sharper perpendicular diffraction peaks after pelletization observed for BO compared to BN, which suggest larger domains and more uniform crystallographic alignment. In contrast, the BN crystallites (Fig. 6b) are generally thicker and exhibit more irregular shapes, including partially fused or aggregated regions, resulting in less clearly defined platelet geometry. Although nanoscale pores are also observed in BN, they occur less frequently and with reduced uniformity compared to BO. This greater variability in particle thickness, lateral dimensions, and aggregation is consistent with the more complex reaction pathway and may contribute to its broader diffraction peaks in certain orientations. Additional lower-magnification SEM images illustrating large-area morphology are provided in SI Fig. S4.

Table 2 SEM-EDS data for BO and BN

Element	BO at%	BN at%	Estimated error %	Theoretical at%
Bi	40.4	40.8	±2.0	40
Te	59.6	59.2	±3.0	60

After consolidation of the polycrystalline powders into pellets *via* hot pressing, cross-sectional SEM imaging of fractured samples was conducted to visually evaluate microstructural differences associated with the preferred orientation inferred from PXRD and corresponding *LF*. Fig. 7a and b present the BO pellet in the perpendicular and parallel viewing directions, respectively, while Fig. 7c and d show the corresponding orientations for BN. In the perpendicular cross-section, BO exhibits densely packed platelet-like crystallites with minimal interparticle void space, consistent with a relatively uniform morphology that promotes efficient stacking and alignment during sintering. In contrast, BN displays a more heterogeneous packing structure with increased voids and irregular stacking, indicative of broader particle size and shape distributions. The BO microstructure further reveals a pronounced degree of crystallite alignment along a common orientation, whereas BN shows a comparatively more random orientation distribution. In the parallel viewing direction, BO again demonstrates relatively uniform morphology and layered stacking, while BN exhibits greater variability in crystallite dimensions and orientation, resulting in a less ordered microstructure overall. These differences in packing behavior are also reflected in the measured pellet densities. While the sintered BO pellet had a measured density of 7.63 g cm^{-3} (approximately 97% of the theoretical density of 7.84 g cm^{-3} for Bi_2Te_3, ICSD 184631), the BN pellet had a lower measured density of 7.19 g cm^{-3} (approximately 92% of theoretical density). The lower densification of BN is therefore consistent with increased residual porosity compared to the more tightly packed BO microstructure.

SEM imaging was also performed to examine the morphology of $Bi_3(C_2H_4O_2)_4NO_3$. As illustrated in Fig. 8a and b, the material crystallizes in the form of well-defined rectangular blocks with flat facets and sharp edges, consistent with the long-range structural ordering observed by SCXRD. At higher magnification (Fig. 8c), the crystal surfaces display numerous fine, needle-like features distributed across the facets. To identify the composition of these surface features, line-scan EDS analysis was conducted, which is shown in SI Fig. S5. As this line scan measures through the needle deep into bulk $Bi_3(C_2H_4O_2)_4NO_3$, its elements remain visible throughout the whole scan. Along a trajectory crossing an individual needle, the weak N and O signals remain relatively constant while the stronger Bi signal decreases over the needle region. Notably, a clear increase in Te intensity coincides with the needle position, despite Te not being a constituent of the Bi-complex. The C spike at the right edge of the scan arises from exposed carbon tape. Together, these observations indicate that the needle-like surface features are composed of elemental tellurium.

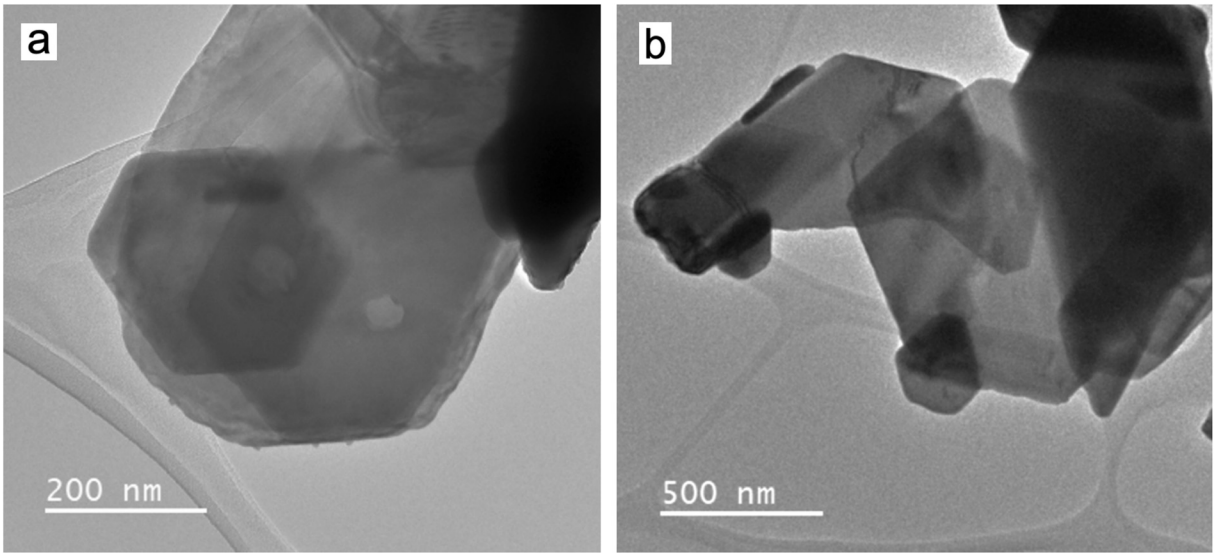

Fig. 6 TEM images for (a) BO and (b) BN.

The presence of Te on the surface of the $Bi_3(C_2H_4O_2)_4NO_3$ crystals suggests that partial $Te^{4+} \rightarrow Te^{2-}$ reduction and Te^0 deposition continue to occur during the BN polyol reaction while the Bi-complex is present. This behaviour aligns with previously proposed growth mechanisms for nanoporous polyol-based Bi_2Te_3 formation, such as that reported by Kimberly *et al.*, in which Bi_2Te_3 initially grows around a central Te nanorod.[18] Then, subsequent dissolution and consumption of the rod results in the formation of voids, consistent with the Kirkendall effect. In the current system, although nanopores are less common in BN compared to BO, some BN crystals still exhibit nanoporous plate morphologies, supporting the possibility that transient Te-rich features contribute to Bi_2Te_3 nucleation and growth in the nitrate-based pathway.

Thermoelectric properties

To assess the influence of bismuth precursor chemistry on thermoelectric performance, the properties of the BO and BN samples are summarized in Fig. 9. As PXRD analysis and cross-sectional SEM photos of the fractured pellets revealed precursor-dependent preferred crystallographic orientation after pelletization, the Seebeck coefficient and electrical conductivity were measured in both the perpendicular (⊥) and parallel (∥) directions relative to the hot-pressing axis. In the plots, filled markers correspond to the perpendicular orientation and hollow markers correspond to the parallel orientation. However, thermal diffusivity was measured only in the parallel direction, the conventional geometry for the laser flash instrument configuration. Consequently, only zT values derived from consistent measurement directions (*i.e.*, parallel) are reported. Moreover, for all measurements, data collected during cooling overlapped with those obtained upon heating, indicating good thermal reversibility and the absence of hysteresis across the investigated temperature range.

The temperature dependence of the electrical conductivity for both BO and BN in Fig. 9a is characteristic of extrinsic narrow gap semiconductors such as Bi_2Te_3. As the temperature begins to increase, the electrical conductivity decreases due to enhanced phonon scattering, which suppresses carrier mobility. At higher temperatures, the curves exhibit a slight upward inflection consistent with the thermal excitation of intrinsic carriers across the small band gap. BO and BN exhibit very comparable electrical conductivity curves, with the BO sample displaying only slightly higher values. At approximately 300 K, the perpendicular electrical conductivity values are 1509 S cm^{-1} for BO and 1414 S cm^{-1} for BN. In the parallel direction, the values are 1327 S cm^{-1} for BO and 1315 S cm^{-1} for BN. These magnitudes fall within the expected range for undoped Bi_2Te_3 synthesized *via* wet-chemical routes. For comparison, Gayner *et al.* reported a perpendicular electrical conductivity of 1189 S cm^{-1} at 302 K for polyol-synthesized Bi_2Te_3 prepared from Bi_2O_3 and Na_2TeO_3.[17] In contrast, Kimberly *et al.* observed a substantially lower parallel electrical conductivity of approximately 556 S cm^{-1} at 323 K for polyol-synthesized Bi_2Te_3 containing large, uniform nanopores prepared from $Bi(NO_3)_3{\cdot}5H_2O$ and Na_2TeO_3, highlighting the strong influence of microstructure on charge transport.[18]

Moreover, both samples exhibit orientation–dependent electrical transport consistent with the preferred crystallographic alignment observed in the pellet PXRD patterns and corroborated by the cross-sectional SEM images. In BO, the electrical conductivity measured parallel to the pressing direction is approximately 13%–14% lower than that measured perpendicular to the pressing direction across the measured temperature range. In contrast, BN displays weaker anisotropy with the parallel conductivity only 5%–8% lower than the perpendicular conductivity, consistent with the less pronounced texturing indicated by the PXRD and SEM results. This directional dependence is consistent with previous studies on solu-

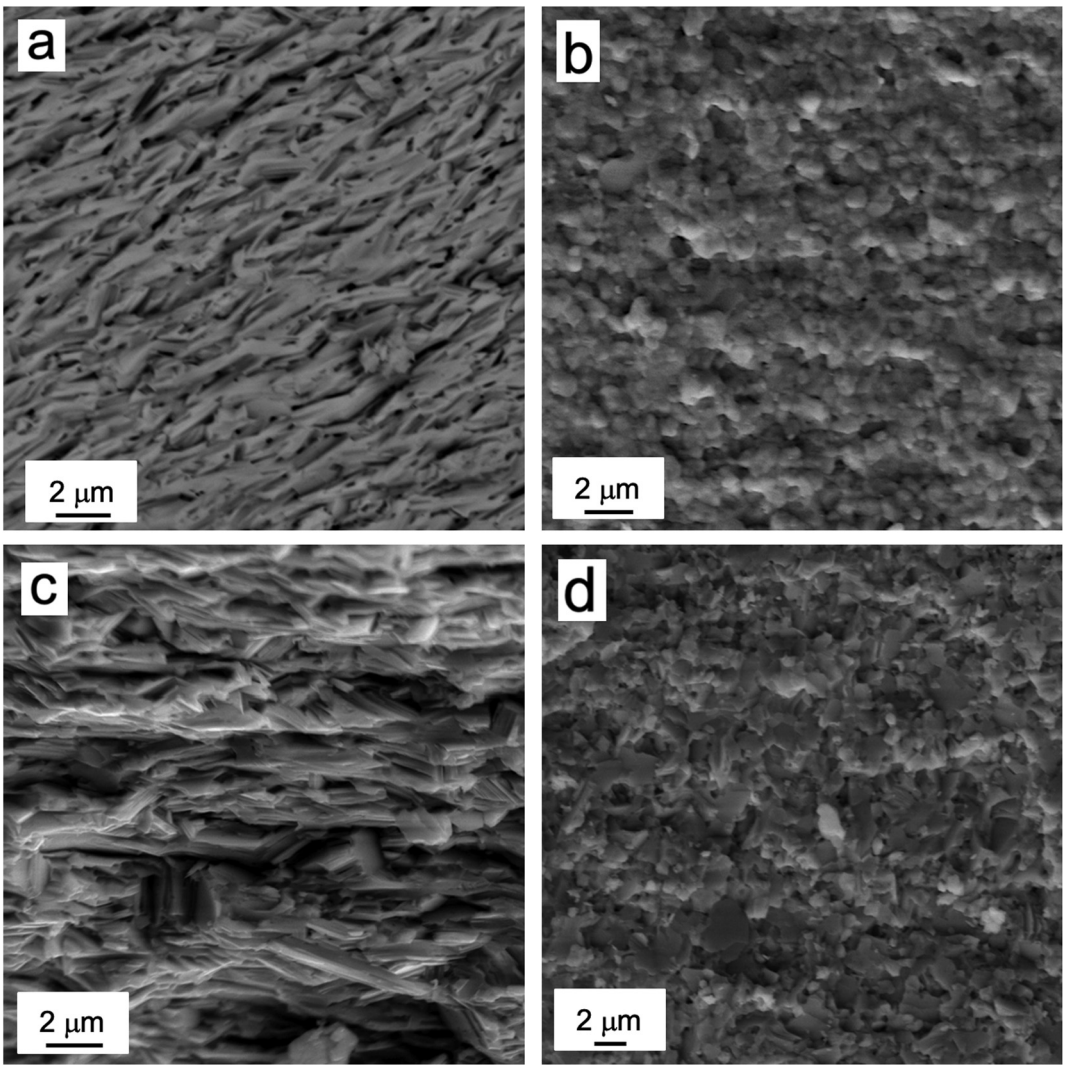

Fig. 7 Cross-sectional SEM images of fractured hot-pressed pellets showing (a) perpendicular and (b) parallel viewing directions for BO, and (c) perpendicular and (d) parallel viewing directions for BN.

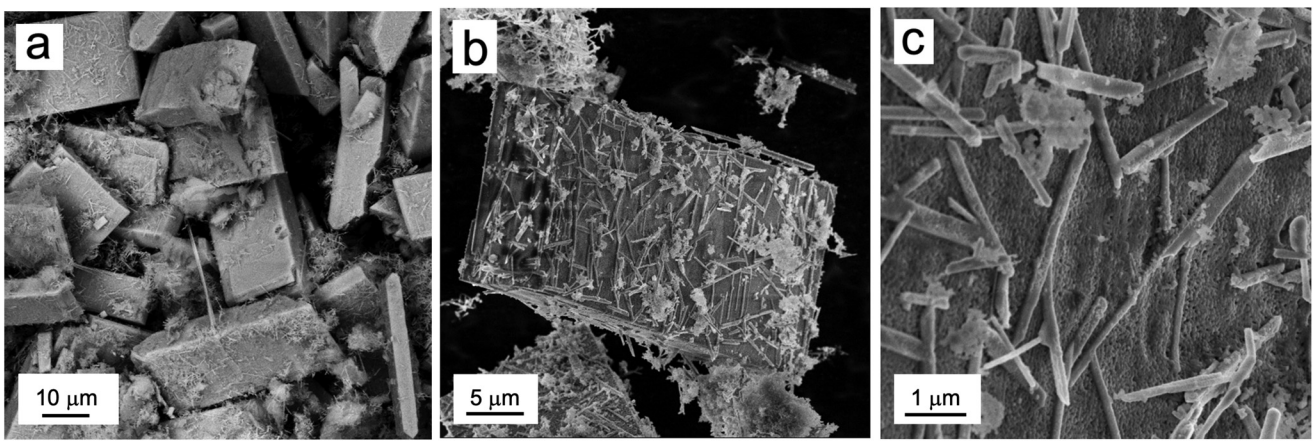

Fig. 8 SEM images of $Bi_3(C_2H_4O_2)_4NO_3$ for (a) a cluster of crystals, (b) a single crystal, and (c) crystal surface.

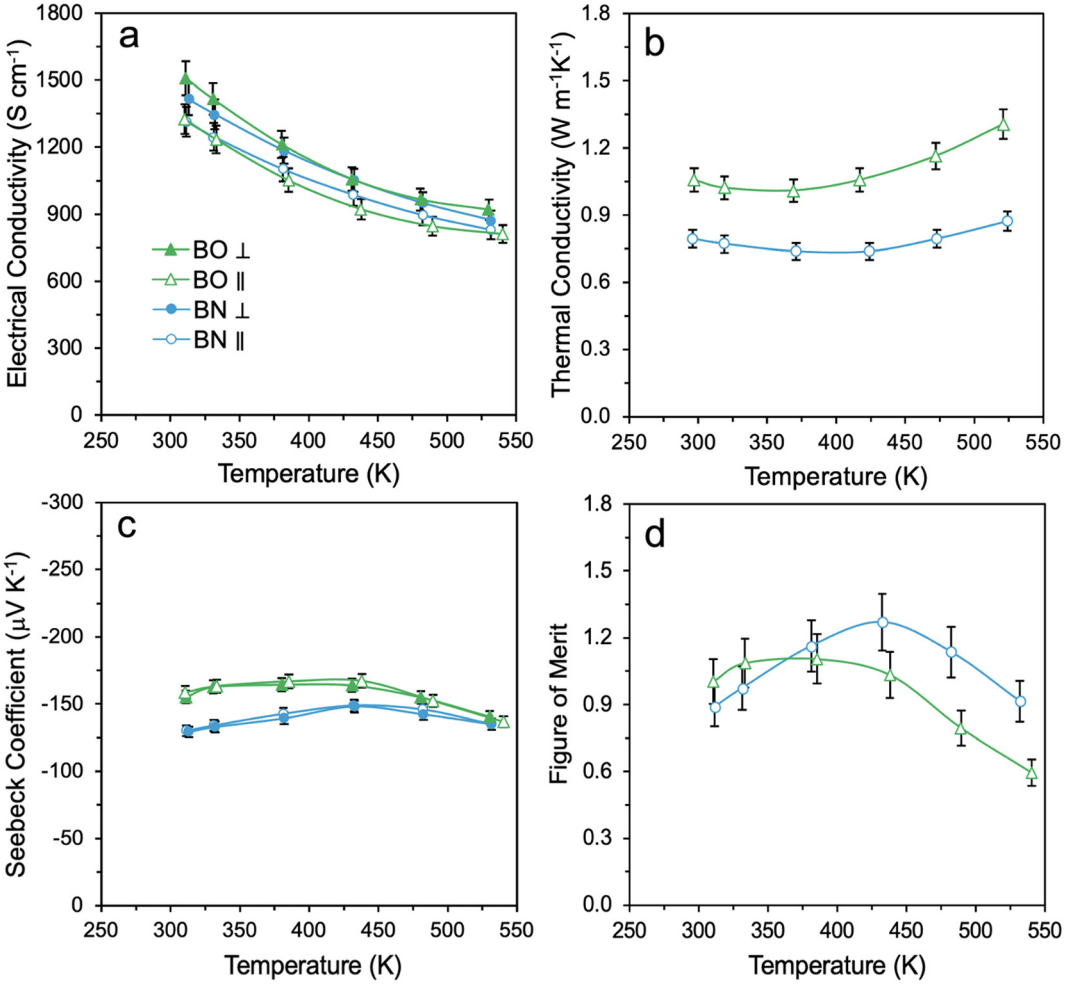

Fig. 9 Thermoelectric properties for BO and BN (a) electrical conductivity (⊥/||), (b) thermal conductivity (||), (c) Seebeck coefficient (⊥/||), and (d) figure of merit (||).

tion-synthesized Bi_2Te_3-based materials[11,18,38] and is typically attributed to the preferential alignment of hexagonal nanoplates during pressing. The nanoplates tend to orient with their basal planes perpendicular to the pressing axis, thus charge transport measured perpendicular to the pressing direction predominantly measures conduction within the Bi_2Te_3 basal planes, where carrier mobility is intrinsically higher. Conversely, transport measured parallel to the pressing direction requires carriers to traverse platelet interfaces and cross the layered Bi_2Te_3 structure, which introduces additional scattering and reduces conductivity. The stronger anisotropy observed in BO correlates with the more pronounced preferred orientation detected in its pellet PXRD patterns and the densely aligned platelet packing observed in cross-sectional SEM images, indicating a higher degree of crystallite alignment. In contrast, BN shows weaker orientation effects and more heterogeneous packing in SEM, suggesting a broader distribution of crystallite orientations. This reduced texturing is consistent with the smaller conductivity differences between the parallel and perpendicular measurement geometries.

Thermal conductivity is the sum of the electronic thermal conductivity (κ_e) and lattice thermal conductivity (κ_l) contributions, as expressed by eqn (6):

$$\kappa = \kappa_e + \kappa_l. \quad (6)$$

The temperature dependence of κ for BO and BN is shown in Fig. 9b, and the corresponding thermal diffusivity ($cm^2\ s^{-1}$) as a function of temperature is presented in SI Fig. S6. Both samples exhibit the expected behaviour for Bi_2Te_3-based semiconductors in which κ initially decreases at lower temperatures due to enhanced phonon scattering. At higher temperatures, however, thermal conductivity increases due to the bipolar effect in which thermally excited minority carriers begin to contribute to heat transport. At approximately 300 K, the measured thermal conductivities are 1.06 W m^{-1} K^{-1} for BO and 0.79 W m^{-1} K^{-1} for BN. These values fall within the typical range for polyol-synthesized Bi_2Te_3-based materials. For example, Gayner *et al.* reported a thermal conductivity of 0.91 W m^{-1} K^{-1} at 303 K synthesized with Bi_2O_3 and Na_2TeO_3 pre-

cursors.[17] In contrast, Kimberly *et al.* achieved a significantly lower thermal conductivity of 0.54 W m^{-1} K^{-1} at 325 K for Bi_2Te_3 synthesized from $Bi(NO_3)_3{\cdot}5H_2O$ and Na_2TeO_3, which was attributed to the presence of large, uniform nanopores that strongly suppress lattice heat transport.[18]

Higher thermal conductivity—with all else being equal—is generally consistent with higher electrical conductivity, since κ_e is proportional to σ according to the Wiedemann–Franz law (eqn (7)):

$$\kappa_e = L\sigma T \tag{7}$$

where, L is the Lorenz number. For metals and highly degenerate semiconductors, the Sommerfeld value ($L_0 = 2.44 \times 10^{-8}$ V^2 K^{-2}) is often used; however, this value overestimates L for extrinsic semiconductors such as the materials in this study. Instead, L is more accurately estimated using the expression in eqn (8):

$$L \approx 1.5 + \exp\left[\frac{-|S|}{116}\right] \tag{8}$$

with S in μV K^{-1} and L in 10^{-8} V^2 K^{-2}.[39] Table 3 summarizes the values of L, κ, κ_e, and κ_l at 300 K for BO and BN in both perpendicular and parallel measurement configurations. The measurement orientation for each quantity is indicated in parentheses: thermal conductivity was only measured parallel to the pressing direction, whereas Seebeck coefficient and electrical conductivity were measured in both orientations. Therefore, κ_l cannot be accurately determined for the perpendicular direction.

Notably, while κ_e is comparable between BO and BN—consistent with their similar electrical conductivity values—BN exhibits a substantially lower κ_l. At 300 K, BN exhibits κ_l = 0.08 W m^{-1} K^{-1}, whereas BO displays a higher value of 0.37 W m^{-1} K^{-1}. Although both values are relatively low, they are comparable to reports for polyol-synthesized Bi_2Te_3 in the literature; for example, Gayner *et al.* and Kimberly *et al.* reported κ_l values of approximately 0.17 W m^{-1} K^{-1} (not corrected for anisotropy) and 0.26 W m^{-1} K^{-1} at 300 K, respectively.[17,18] Several factors rooted in the microstructural variations between the two materials in this study likely contribute to the reduced lattice contribution in BN. TEM imaging shows that BN crystallites are generally more irregular and contain a broader distribution of morphological features than the comparatively uniform nanoplatelets observed in BO. Such structural heterogeneity increases phonon scattering through a combination of higher grain-boundary density, nonuniform platelet stacking, and complex platelet-aggregate interfaces. Cross-sectional SEM of fractured pellets further corroborates this by revealing that BN possesses more heterogeneous packing with increased void space, consistent with its lower measured density (7.19 g cm^{-3}, ~92% of theoretical) compared to BO (7.63 g cm^{-3}, ~97% of theoretical). This higher apparent porosity in BN introduces additional phonon-scattering at pore interfaces and platelet boundaries, contributing directly to suppression of lattice heat transport. PXRD data also support this interpretation: in pellet form, BN exhibits broader diffraction peaks in the perpendicular orientation, consistent with smaller coherent domain sizes and elevated microstrain, both of which suppress phonon mean free paths. Additionally, the BN synthesis proceeds through multiple phase formations, including the formation of $Bi_3(C_2H_4O_2)_4NO_3$. This multistep pathway introduces additional microstructural disorder, residual strain, and/or point-defect populations relative to the more direct BO route. Together, these effects significantly impede phonon transport, explaining the substantially lower κ_l in BN even though the two samples exhibit broadly comparable electronic transport properties.

The Seebeck coefficient curves shown in Fig. 9c exhibit the expected temperature dependence for Bi_2Te_3, first increasing in magnitude with temperature before decreasing at higher temperatures due to the bipolar effect. At approximately 300 K, BO has Seebeck coefficients of −155 μV K^{-1} (⊥) and −159 μV K^{-1} (∥), whereas BN exhibits values of −129 μV K^{-1} (⊥) and −130 μV K^{-1} (∥). These magnitudes are in good agreement with previously reported values for polyol-synthesized Bi_2Te_3. For example, Gayner *et al.* reported a Seebeck coefficient of −125 μV K^{-1} at 303 K for Bi_2Te_3 synthesized using Bi_2O_3 and Na_2TeO_3,[17] while Kimberly *et al.* obtained −126 μV K^{-1} at 322 K for Bi_2Te_3 prepared from $Bi(NO_3)_3{\cdot}5H_2O$ and Na_2TeO_3 precursors.[18]

In simple models, the Seebeck coefficient and electrical conductivity are often inversely correlated due to the opposite dependencies on charge carrier concentration. However, this inverse relation only holds when the carrier concentration is the dominant variable. Compared to BN, the BO sample exhibits both slightly higher electrical conductivity (*e.g.*, 1%–7% depending on orientation at 300 K) and significantly larger absolute Seebeck coefficient (*e.g.*, 18%–20% at 300 K), suggesting differences in charge carrier mobility between the two materials. Structural characterization *via* PXRD, SEM, and TEM shows that BO possesses improved crystallinity, more uniform platelet morphology, and reduced microstructural disorder relative to BN, all of which are consistent with reduced carrier scattering and enhanced mobility. To verify this interpretation, Hall measurements were conducted to experimentally determine carrier concentration and mobility, the results of which are displayed in Table 4.

Hall measurements summarized in Table 4 confirm that BO exhibits substantially higher charge carrier mobility than BN, almost twice as high with values of 194 cm^2 V^{-1} s^{-1} and 109 cm^2 V^{-1} s^{-1}, respectively. Furthermore, despite nearly

Table 3 L, κ, κ_e, and κ_l of BO (⊥/∥)[a] and BN (⊥/∥)[a] at 300 K

Sample	L (10^{-8} V^2 K^{-2})	κ (W m^{-1} K^{-1})	κ_e (W m^{-1} K^{-1})	κ_l (W m^{-1} K^{-1})
BO ⊥	1.76 (⊥)	—	0.79 (⊥)	—
BO ∥	1.75 (∥)	1.06 (∥)	0.69 (∥)	0.37 (∥–∥)
BN ⊥	1.83 (⊥)	—	0.76 (⊥)	—
BN ∥	1.83 (∥)	0.79 (∥)	0.71 (∥)	0.08 (∥–∥)

[a] Measurement directions noted in parentheses.

Table 4 BO and BN Hall carrier mobility and concentration at room temperature

Sample	BO (⊥)	BN (⊥)
Carrier mobility μ ($cm^2\ V^{-1}\ s^{-1}$)	194	109
Carrier concentration n ($10^{19}\ cm^{-3}$)	−4.61	−6.07

identical compositions determined by EDS, BN shows a 32% higher carrier concentration ($6.07 \times 10^{19}\ cm^{-3}$) compared with BO ($4.61 \times 10^{19}\ cm^{-3}$). In undoped Bi_2Te_3, carrier concentration is governed primarily by intrinsic point defects, particularly antisite defects and Te vacancies, which are sensitive to synthesis pathway and microstructural disorder. The combination of higher carrier concentration and lower mobility in BN yields electrical conductivity values comparable to those of BO, consistent with the relationship outlined in eqn (9). However, reduced mobility and increased carrier concentration in BN contribute to a smaller absolute value of the Seebeck coefficient. In contrast, BO maintains higher mobility without a proportional increase in carrier density. Consequently, BO achieves basically equivalent electrical conductivity along with an enhanced Seebeck coefficient, highlighting the role of microstructure-driven transport differences between the two materials.

Eqn (9) expresses electrical conductivity as the product of carrier concentration (n), the charge of an electron (e), and the carrier mobility (μ):

$$\sigma = n \cdot e \cdot \mu. \quad (9)$$

Moreover, electrical conductivity is much more anisotropic than Seebeck coefficient because the mobility is highly sensitive to crystallographic texture, platelet alignment, and grain-boundary density, all of which differ between orientations as revealed by pellet PXRD and SEM. In contrast, the Seebeck coefficient depends more strongly on carrier concentration and the Density Of States, which are essentially invariant with respect to measurement direction. As a result, both BO and BN display only minor orientation-dependent variations in Seebeck coefficient.

Lastly, the figure of merit curves in Fig. 9d exhibit the expected trend, showing an initial rise followed by a decline at higher temperatures due to the bipolar effect. The BO and BN samples display comparable overall performance, with differences that reflect their precursor-dependent microstructural and transport characteristics. When measured in the parallel direction—which corresponds to the geometry used for thermal diffusivity—BO exhibits a peak zT of 1.10 at 333 K and an average zT of 0.94 between 310 K–540 K, while BN reaches a superior peak of 1.27 at 432 K with a superior average of 1.06 between 311 K–532 K. These values are consistent with literature reports for polyol-synthesized Bi_2Te_3. For example, Gayner *et al.*, achieved a peak "zT" of 1.30 at 450 K and an average "zT" of 1.14 between 300 K–500 K for Bi_2Te_3 synthesized from Bi_2O_3 and Na_2TeO_3 precursors.[17] Moreover, Kimberly *et al.* obtained a peak zT of 0.75 at 425 K and an average zT of 0.65 from 300 K–500 K for Bi_2Te_3 synthesized using $Bi(NO_3)_3{\cdot}5H_2O$ and Na_2TeO_3.[18] Notably, the peak zT of BO occurs at a lower temperature, suggesting that it may be more suitable for low- or room-temperature waste-heat or cooling applications, whereas BN performs slightly better at elevated temperatures. These results reinforce that precursor-dependent microstructure and texturing have measurable consequences for thermoelectric transport and must be considered when optimizing polyol synthesis routes for targeted operating temperatures and anisotropic performance requirements.

Conclusions

In this study, two polyol-based synthesis routes for Bi_2Te_3 were systematically examined using Bi_2O_3 and $Bi(NO_3)_3{\cdot}5H_2O$ as bismuth precursors, revealing distinct precursor-dependent reaction pathways, structural features, and thermoelectric behaviors. While the Bi_2O_3 route converted directly to Bi_2Te_3, the $Bi(NO_3)_3{\cdot}5H_2O$ route proceeded through Bi_2TeO_5 followed by the formation of a previously unreported bismuth-ethylene glycolate-nitrate complex, $Bi_3(C_2H_4O_2)_4NO_3$. The structural features of the newly identified Bi complex were characterized and contextualized within the overall reaction pathway. Moreover, comparative analysis of the resulting Bi_2Te_3 powders and pellets demonstrated that precursor chemistry influences microstructure, domain size, and the extent of preferred orientation induced during pelletization, which in turn affects electrical and thermal transport. Despite these differences, both BO and BN samples exhibited comparable thermoelectric properties, though with measurable variations in anisotropy and temperature-dependent performance. Specifically, the performance of BN was superior, with an average zT of 1.06 between 311 K–532 K, compared to 0.94 between 310 K–540 K for BO. Overall, these findings highlight the critical role of precursor selection in governing phase formation, microstructural development, and thermoelectric performance in solution-synthesized Bi_2Te_3, providing valuable insight for the rational design and optimization of polyol-based thermoelectric materials.

Author contributions

Made substantial contributions to conception and design of the study: Donohoe, M., Licskai, T.; performed data acquisition, analysis, and interpretation: Donohoe, M., Licskai, T., Niknam, E., Assoud, A., Zou, T., Kycia, J.; drafted the work or substantively revised it: Donohoe, M., Licskai, T., Kleinke, H.; provided administrative, technical, and material support: Kleinke, H.

Conflicts of interest

There are no conflicts to declare.

Data availability

The data supporting this article have been included as part of the supplementary information (SI). Supplementary information is available. See DOI: https://doi.org/10.1039/d5nr05277g.

CCDC 2516205 ($Bi_3(C_2H_4O_2)_4NO_3$) contains the supplementary crystallographic data for this paper.[40]

Acknowledgements

The authors gratefully acknowledge the use of the University of Waterloo's QNFCF and WATLab facilities for TEM and SEM imaging, respectively, and thank the staff for their support and expertise. This work was supported by New Frontiers in Research Fund (NFRFE-2021-00435).

References

1 R. Freer and A. V. Powell, *J. Mater. Chem. C*, 2020, **8**, 441–463, DOI: 10.1039/c9tc05710b.
2 H. Park, D. Lee, G. Park, S. Park, S. Khan, J. Kim and W. Kim, *JPhys Energy*, 2019, **1**, 042001, DOI: 10.1088/2515-7655/ab2f1e.
3 E. W. Zaia, M. P. Gordon, P. Yuan and J. J. Urban, *Adv. Electron. Mater.*, 2019, **5**, 1–20, DOI: 10.1002/aelm.201800823.
4 L. Francioso, C. De Pascali, I. Farella, C. Martucci, P. Cret, P. Siciliano and A. Perrone, *J. Power Sources*, 2011, **196**, 3239–3243, DOI: 10.1016/j.jpowsour.2010.11.081.
5 M. A. Zoui, S. Bentouba, J. G. Stocholm and M. Bourouis, *Energies*, 2020, **13**, 3606, DOI: 10.3390/en13143606.
6 Z. Liu, B. Tian, Y. Li, Z. Guo, Z. Zhang, Z. Luo, L. Zhao, Q. Lin, C. Lee and Z. Jiang, *Small*, 2023, **19**, 2304599, DOI: 10.1002/smll.202304599.
7 N. Jaziri, A. Boughamoura, J. Müller, B. Mezghani, F. Tounsi and M. Ismail, *Energy Rep.*, 2020, **6**, 264–287, DOI: 10.1016/j.egyr.2019.12.011.
8 P. He and Y. Wu, *Nano Res.*, 2021, **14**, 3608–3615, DOI: 10.1007/s12274-021-3555-0.
9 K. T. Lee, D. S. Lee, W. H. Chen, Y. L. Lin, D. Luo, Y. K. Park and A. Bandala, *iScience*, 2023, **26**, 107874, DOI: 10.1016/j.isci.2023.107874.
10 V. V. Atuchin, T. A. Gavrilova, K. A. Kokh, N. V. Kuratieva, N. V. Pervukhina and N. V. Surovtsev, *Solid State Commun.*, 2012, **152**, 1119–1122, DOI: 10.1016/j.ssc.2012.04.007.
11 M. Donohoe, E. Niknam, T. Zou, J. Kycia and H. Kleinke, *Chem. Mater.*, 2025, **37**, 9429–9439, DOI: 10.1021/acs.chemmater.5c01841.
12 G. S. Hegde and A. N. Prabhu, *J. Electron. Mater.*, 2022, **51**, 2014–2042, DOI: 10.1007/s11664-022-09513-x.
13 N. Nandihalli, *Crit. Rev. Solid State Mater. Sci.*, 2023, **48**, 361–410, DOI: 10.1080/10408436.2022.2053499.
14 T. Lu, L. Chen, X. Shi, W. Liu, M. Li, Y. Wang, X. Zeng, P. Song, J. Bell, G. J. Snyder, Z. Chen and M. Hong, *Small Struct.*, 2025, **6**, 2400694, DOI: 10.1002/sstr.202400694.
15 N. Nandihalli, D. H. Gregory and T. Mori, *Adv. Sci.*, 2022, **9**, 2106052, DOI: 10.1002/advs.202106052.
16 C. Fiedler, T. Kleinhanns, M. Garcia, S. Lee, M. Calcabrini and M. Ibáñez, *Chem. Mater.*, 2022, **34**, 8471–8489, DOI: 10.1021/acs.chemmater.2c01967.
17 C. Gayner, L. T. Menezes, Y. Natanzon, Y. Kauffmann, H. Kleinke and Y. Amouyal, *ACS Appl. Mater. Interfaces*, 2023, **15**, 13012–13024, DOI: 10.1021/acsami.2c21561.
18 T. Q. Kimberly, E. Y. C. Wang, G. D. Navarro, X. Qi, K. M. Ciesielski, E. S. Toberer and S. M. Kauzlarich, *Chem. Mater.*, 2024, **36**, 6618–6626, DOI: 10.1021/acs.chemmater.4c01092.
19 B. H. Toby and R. B. Von Dreele, *J. Appl. Crystallogr.*, 2013, **46**, 544–549, DOI: 10.1107/S0021889813003531.
20 D. Liu, X. Li, P. M. De Castro Borlido, S. Botti, R. Schmechel and M. Rettenmayr, *Sci. Rep.*, 2017, **7**, 43611, DOI: 10.1038/srep43611.
21 W. Liu, K. C. Lukas, K. McEnaney, S. Lee, Q. Zhang, C. P. Opeil, G. Chen and Z. Ren, *Energy Environ. Sci.*, 2013, **6**, 552–560, DOI: 10.1039/c2ee23549h.
22 H. Wang, W. D. Porter, H. Böttner, J. König, L. Chen, S. Bai, T. M. Tritt, A. Mayolet, J. Senawiratne, C. Smith, F. Harris, P. Gilbert, J. Sharp, J. Lo, H. Kleinke and L. Kiss, *J. Electron. Mater.*, 2013, **42**, 1073–1084, DOI: 10.1007/s11664-013-2516-0.
23 H. Wang, W. D. Porter, H. Böttner, J. König, L. Chen, S. Bai, T. M. Tritt, A. Mayolet, J. Senawiratne, C. Smith, F. Harris, P. Gilbert, J. W. Sharp, J. Lo, H. Kleinke and L. Kiss, *J. Electron. Mater.*, 2013, **42**, 654–664, DOI: 10.1007/s11664-012-2396-8.
24 P. Giannozzi, O. Andreussi, T. Brumme, O. Bunau, M. B. Nardelli, M. Calandra, R. Car, C. Cavazzoni, D. Ceresoli, M. Cococcioni, N. Colonna, I. Carnimeo, A. Dal Corso, S. De Gironcoli, P. Delugas, R. A. Distasio, A. Ferretti, A. Floris, G. Fratesi, G. Fugallo, R. Gebauer, U. Gerstmann, F. Giustino, T. Gorni, J. Jia, M. Kawamura, H. Y. Ko, A. Kokalj, E. Kücükbenli, M. Lazzeri, M. Marsili, N. Marzari, F. Mauri, N. L. Nguyen, H. V. Nguyen, A. Otero-De-La-Roza, L. Paulatto, S. Poncé, D. Rocca, R. Sabatini, B. Santra, M. Schlipf, A. P. Seitsonen, A. Smogunov, I. Timrov, T. Thonhauser, P. Umari, N. Vast, X. Wu and S. Baroni, *J. Phys. Condens. Matter*, 2017, **29**, 465901, DOI: 10.1088/1361-648X/aa8f79.
25 P. Giannozzi, O. Baseggio, P. Bonfà, D. Brunato, R. Car, I. Carnimeo, C. Cavazzoni, S. De Gironcoli, P. Delugas, F. F. Ruffino, A. Ferretti, N. Marzari, I. Timrov, A. Urru and S. Baroni, *J. Chem. Phys.*, 2020, **152**, 154105, DOI: 10.1063/5.0005082.
26 P. Giannozzi, S. Baroni, N. Bonini, M. Calandra, R. Car, C. Cavazzoni, D. Ceresoli, G. L. Chiarotti, M. Cococcioni, I. Dabo, A. Dal Corso, S. de Gironcoli, S. Fabris, G. Fratesi, R. Gebauer, U. Gerstmann, C. Gougoussis, A. Kokalj, M. Lazzeri, L. Martin-Samos, N. Marzari, F. Mauri,

R. Mazzarello, S. Paolini, A. Pasquarello, L. Paulatto, C. Sbraccia, S. Scandolo, G. Sclauzero, A. P. Seitsonen, A. Smogunov, P. Umari and R. M. Wentzcovitch, *J. Phys. Condens. Matter*, 2009, **21**, 395502, DOI: 10.1088/0953-8984/21/39/395502.

27 J. P. Perdew, K. Burke and M. Ernzerhof, *Phys. Rev. Lett.*, 1996, **77**, 3865–3868, DOI: 10.1103/PhysRevLett.77.3865.

28 H. Yamazaki, R. Eguchi and M. Takashiri, *Cryst. Res. Technol.*, 2021, **56**, 2100153, DOI: 10.1002/crat.202100153.

29 Y. Wang, W. Di Liu, H. Gao, L. J. Wang, M. Li, X. L. Shi, M. Hong, H. Wang, J. Zou and Z. G. Chen, *ACS Appl. Mater. Interfaces*, 2019, **11**, 31237–31244, DOI: 10.1021/acsami.9b12079.

30 G. M. Park, S. Lee, J. Y. Kang, S. H. Baek, H. Kim, J. S. Kim and S. K. Kim, *J. Adv. Ceram.*, 2023, **12**, 2360–2370, DOI: 10.26599/JAC.2023.9220825.

31 K. Momma and F. Izumi, *J. Appl. Crystallogr.*, 2008, **41**, 653–658, DOI: 10.1107/S0021889808012016.

32 F. Lazarini, *Acta Crystallogr. B.*, 1979, **35**, 448–450, DOI: 10.1107/s0567740879003745.

33 S. M. Biros, B. M. Bridgewater, A. Villeges-Estrada, J. M. Tanski and G. Parkin, *Inorg. Chem.*, 2002, **41**, 4051–4057, DOI: 10.1021/ic020204b.

34 T. Q. Kimberly, K. M. Ciesielski, X. Qi, E. S. Toberer and S. M. Kauzlarich, *ACS Appl. Electron. Mater.*, 2024, **6**, 2816–2825, DOI: 10.1021/acsaelm.3c00385.

35 C. Dun, C. A. Hewitt, Q. Jiang, Y. Guo, J. Xu, Y. Li, Q. Li, H. Wang and D. L. Carroll, *Chem. Mater.*, 2018, **30**, 1965–1970, DOI: 10.1021/acs.chemmater.7b04985.

36 A. Soni, Z. Yanyuan, Y. Ligen, M. K. K. Aik, M. S. Dresselhaus and Q. Xiong, *Nano Lett.*, 2012, **12**, 1203–1209, DOI: 10.1021/nl2034859.

37 R. Furushima, S. Tanaka, Z. Kato and K. Uematsu, *J. Ceram. Soc. Jpn.*, 2010, **118**, 921–926, DOI: 10.2109/jcersj2.118.921.

38 X. Yan, B. Poudel, Y. Ma, W. S. Liu, G. Joshi, H. Wang, Y. Lan, D. Wang, G. Chen and Z. F. Ren, *Nano Lett.*, 2010, **10**, 3373–3378, DOI: 10.1021/nl101156v.

39 H. S. Kim, Z. M. Gibbs, Y. Tang, H. Wang and G. J. Snyder, *APL Mater.*, 2015, **3**, 041506, DOI: 10.1063/1.4908244.

40 CCDC 2516205: Experimental Crystal Structure Determination, 2026, DOI: 10.5517/ccdc.csd.cc2qg9xf.